GSA DATA REPOSITORY 2011201 **Butler et al.**

SUPPLEMENTARY INFORMATION ON NUMERICAL MODELLING APPROACH

The present models employ the same numerical approach and philosophy used in our most recent work. Below we describe this approach following Beaumont et al. (2009), except where noted.

Explanation of Nested Version of Sopale Software

Sopale Nested is a version of the plane strain arbitrary Lagrangian Eulerian (ALE) software Sopale (Fullsack, 1995) that solves thermal-mechanical creeping flows in a large-scale (LS) domain that contains a second, higher-resolution (small-scale or SS) sub-domain (Figure DR1). In the current models the LS grid has a maximum resolution (in the lithosphere) of 10 x 2 km (10 x 10 km in the sublithosphere), while the SS grid, positioned in the vicinity of the subduction zone (from 400 to 1400 km wide and 190 km deep) has a resolution of 2 x 2 km. The purpose of this approach is to achieve a high-resolution solution while minimizing computational requirements by solving the problem sequentially, first for the entire LS domain (including the SS domain) and then again at a higher resolution for the SS domain using boundary conditions derived from the LS solution. The grid for the SS domain is defined by increasing the resolution of the LS grid by multiples of m and n in the horizontal and vertical directions. This means that the LS grid in the SS domain is the SS grid reduced by removing all but multiples of every m^{th} and n^{th} column and row. The two domains share a single cloud of Lagrangian tracking particles that has a high uniform density distribution throughout the model domain, sufficient that the model geometry and properties can be advected through both the LS and SS domains without loss of fidelity. The initial conditions are defined for the entire model and then transferred to the LS and SS domains. For each timestep the nonlinear problem is solved iteratively for the LS domain using the LS boundary conditions. The velocity and temperature from the LS solution at nodes corresponding to the boundaries of the SS domain are then interpolated onto the boundary nodes of the SS domain, and the problem is solved iteratively for the SS domain at the higher resolution. Finally, the Lagrangian particle positions and properties are updated using the LS and SS solutions for their respective domains. Coupling between the LS and SS domains is achieved by the replacement of the LS solution by the SS solution within the SS domain. The solutions do not drift apart because the Lagrangian cloud, which defines the material properties, is shared between the two grids. This means that particles used to track material properties (e.g., pressure, temperature, etc.) record the LS solution when they are outside of the SS domain, and the SS solution when they are inside.

Governing Equations

For each timestep, the models solve the equations for incompressible creeping (Stokes) flow (Eqs. 1 and 2) and energy balance (Eq. 3) in the LS and SS model domains:

$$\frac{\partial \sigma_{ij}}{\partial x_i} - \frac{\partial P}{\partial x_j} + \rho g = 0 \qquad i,j = 1,2, \qquad \text{(Eq. 1)}$$

$$\frac{\partial v_i}{\partial x_i} = 0 \quad i=1,2, \qquad \text{(Eq. 2)}$$

$$\rho c_p \left(\frac{\partial T}{\partial t} + v_i \frac{\partial T}{\partial x_i} \right) = K \frac{\partial}{\partial x_i} \frac{\partial T}{\partial x_i} + A + A_{SH} + v_2 \alpha g T \rho \qquad i=1,2, \qquad \text{(Eq. 3)}$$

where σ_{ij} is the deviatoric stress tensor, x_i are the spatial coordinates, P pressure, ρ density, g gravitational acceleration, v_i a component of velocity, c_p specific heat, T temperature, t time, K thermal conductivity, A radioactive heat production per unit volume, A_{SH} shear heating, and α volumetric expansivity. Most of the parameter values vary according to the type of material. The last term in the heat balance equation is the temperature correction for adiabatic heating when material moves vertically at velocity v_2. During phase transitions incompressibility (Eq. 2) is replaced by mass conservation (see below).

Boundary and Initial Conditions

The initial steady-state temperature field is calculated at the model scale, with 0°C surface temperature, insulated side boundaries, radioactive heating (Fig. DR1; Table DR1), and a basal heat flux of 20.8 mW/m^3. For the continental interiors this gives a Moho temperature of 570°C, a basal lithosphere temperature of 1336°C, and corresponding surface heat flow (55 mW/m^3) typical of old continental lithosphere. The sublithospheric mantle has a high thermal conductivity to maintain a heat flux and an adiabatic temperature gradient of 0.3 K/km, as expected of a convecting mantle.

The model has a free upper surface and no-slip sides and base. Procontinent material enters the system at a velocity of 2.5 cm/a (5 cm/a during oceanic subduction) along the right side of the model domain, and is balanced by a small outward flow of material below the lithosphere on both sides of the model. This outward flow is further modulated to keep the model in constant isostatic equilibrium and to ensure the surface remains balanced with the upper mantle outside the domain by maintaining an average pressure at the base of the model.

Subduction in the models is initiated dynamically in response to the velocity boundary conditions by the inclusion of a small weak zone embedded at the boundary between the oceanic and stationary retrocontinent lithosphere (Fig. 2, DR1). The inclusion of this weak zone minimizes the mechanical coupling between the two plates during the subduction initiation stage.

However, on the longer term the style of subduction in the models (e.g., slab dip, degree of retromantle deformation, etc.) is dynamic, apart from the velocity boundary conditions. The models presented here were purposely designed to involve a one-sided style of subduction (similar to the weakly coupled models of Faccenda et al., 2008).

Model Properties

The model materials have both plastic (brittle) and viscous (power law creep) properties. Drucker-Prager frictional-plastic yielding occurs when

$$(J_2')^{1/2} = C \cos \varphi_{\text{eff}} + P \sin \varphi_{\text{eff}} \qquad \text{(Eq. 4)}$$

where J_2' is the second invariant of the deviatoric stress, P the dynamical pressure (mean stress), and C the cohesion. The effective internal angle of friction, φ_{eff} is defined to include the effects of pore fluid pressures through the approximate relation

$$P \sin \varphi_{\text{eff}} = (P - P_f) \sin \varphi \qquad \text{(Eq. 5)}$$

where $\varphi = 30°$ is the internal angle of friction for dry conditions ($P_f = 0$). φ_{eff} is an apparent internal angle of friction of the material owing to pore fluid pressure and/or strain softening (see below). For all normal model materials except the weak zone (Fig. DR1), $\varphi_{\text{eff}} = 15°$, approximating hydrostatic fluid pressures. The weak zone material used to initiate subduction has $\varphi_{\text{eff}} = 5°$. The φ_{eff} of the retrocontinent margin crust is reduced from 15° to 7° in the model R in order to represent preexisting weakness.

For incompressible power-law flow, the effective viscosity is:

$$\eta_{\text{eff}}^{v} = \frac{f}{W} B^* \dot{I}_2'^{(1-n)/2n} \exp\left(\frac{Q + PV^*}{nRT_K}\right) \qquad \text{(Eq. 6)}$$

where f is a viscosity scaling factor, W is a strain-weakening factor (see below), B^* is the pre-exponential factor, converted to the tensor invariant form (Table DR1), $\dot{I}_2'$ is the second invariant of the deviatoric strain rate, n is the stress exponent, Q is the activation energy, P is the pressure, V^* is the activation volume for power-law creep, T_K is the absolute temperature and R is the universal gas constant.

The viscous flow laws for the model materials are based on a small set of reliable laboratory flow laws in order to keep the models as simple as possible and facilitate

interpretation. These include Wet Quartzite for the upper/middle crust (WQ; melt-absent Black Hills Quartzite; Gleason and Tullis, 1995), Dry Maryland Diabase for the lower crust (DMD; Mackwell et al., 1998), and Wet Olivine for the mantle lithosphere and asthenosphere (WO; Karato and Wu, 1993). The values of B^* from these flow laws are scaled linearly by the factor f to represent materials that are either stronger or weaker than the base flow law, dry vs. wet conditions, or moderate changes in composition (Beaumont et al., 2006; Warren et al., 2008a,b). This scaling helps to minimize the number of sources of error while allowing some variation in the flow properties, simplifies the interpretation of model results, and acknowledges uncertainties in the composition and rheological properties of Earth. The choice of reference flow law does not imply that the corresponding Earth material has the composition of the reference material.

In the present models the procontinent and retrocontinent margins have a WQ rheology with $f = 3$ (2 in Model R), representing a quartz-dominated crust somewhat stronger than the base WQ flow law, while the overlying sediments have a WQ, $f = 1$ flow law. The continental interiors have a WQ, $f = 5$ rheology, representing refractory/depleted continental crust. The lower and oceanic crust both have a DMD, $f = 0.1$ rheology, corresponding to the rheology of intermediate granulite (Mackwell et al., 1998). The mantle lithospheres have a depleted WO flow law with $f = 10$, and the sublithospheric mantle has a WO flow law with $f = 1$.

Strain Softening and Weakening

The crustal materials undergo a parametric weakening in both the frictional-plastic and ductile regimes (Huismans and Beaumont, 2003; Sobolev and Babeyko, 2005; Warren et al., 2008a,b), termed "softening" and "weakening" respectively.

Frictional-plastic materials strain-soften through a linear decrease in the effective internal angle of friction, φ_{eff} with accumulated plastic strain: $\varphi_{eff} = \varphi_{eff}(I_2'^{1/2})$. $I_2^{1/2} = \varepsilon$ is the square root of the second invariant of deviatoric strain, with ε ("strain") used for simplicity. This approach approximates deformation-induced mechanical or pore-fluid pressure softening of faults and brittle shear zones. In the current models, for all model materials apart from the weak zone and sediments, φ_{eff} is reduced from 15^o to 2^o (or 7^o to 2^o for the retrocontinent margin crust in model R) over $0.5 \leq \varepsilon \leq 1.5$ (Huismans and Beaumont, 2003). The weak zone is modeled as an initially weak region, $\varphi_{eff} = 5^o$, inherited from earlier deformation. The sediments have $\varphi_{eff} = 5^o$ to 2^o.

Viscous strain weakening, representing the combined effects of reaction- and strain-weakening mechanisms during ductile deformation, proceeds through a linear decrease in effective viscosity by the factor $W = 10$ over the range $5 \leq \varepsilon \leq 10$ for all crustal materials in the current models. The mantle lithosphere and sublithospheric mantle materials do not undergo strain weakening in the models. Previous work has tested the sensitivity of similar models to

variations in the strain weakening factor from $W = 1$ to $W = 100$ over the range $5 \leq \varepsilon \leq 10$ (Warren et al., 2008a), and in the strain weakening range, from $0.5 \leq \varepsilon \leq 1$, and $2 \leq \varepsilon \leq 5$ at $W = 10$ (Warren et al., 2008b).

Density, Volume, and Mass Conservation During Phase Transitions

The model crustal materials increase and decrease in density and volume at pressure and temperature conditions corresponding to metamorphic phase changes (Table DR1; Warren et al., 2008a). The densities of lower continental and oceanic crust change across the eclogite field boundary from 2950 to 3100 km/m^3 and from 2900 to 3300 kg/m^3 respectively, on the assumption that the oceanic crust is more mafic than the assumed intermediate composition lower continental crust. The density of the upper crust changes from 2800 to 2850 (HP) to 2900 kg/m^3 (UHP), on the assumption that it consists of 10% mafic and 90% felsic material by volume and that all quartz transforms to coesite at UHP conditions. These density changes reverse during exhumation.

During these phase changes the incompressibility equation is modified to that of mass conservation: $\partial\rho/\partial t = -\partial(\rho v_i)/\partial x_i$. This accounts for the associated volume change and its effect on the buoyancy and velocity field. This volume change is calculated numerically by applying additional normal, compressive/dilatational forces to finite elements at the time they are subject to phase-related density changes. The value of the excess pressure is $\Delta P = \Delta\rho/\beta_v\rho$, where β_v is the viscous bulk modulus of the material, and $\Delta\rho/\rho$ is the fractional change in density corresponding to the phase change. The excess pressure compresses material locally and only during the model time steps when the phase changes occur, thereby ensuring mass conservation. The fractional volume change accompanying a phase change is small in these models and its effect on the velocity field is minor because it only applies at the time of the phase change. However, failure to ensure mass conservation would have a long-term effect on the model because the buoyancy forces will be over- or under-estimated by the fractional error in the material volume.

References

Beaumont, C., Nguyen, M.H., Jamieson, R.A., and Ellis, S. 2006. Crustal flow modes in large hot orogens. In: R.D. Law, M.P. Searle and L. Godin, Editors, Channel Flows, Ductile Extrusion and Exhumation in Continental Collision Zones, Geological Society of London Special Publication 268 (2006), p. 91-145.

Beaumont, C., Jamieson, R.A., Butler, J.P., Warren, C.J. 2009. Crustal structure: A key constraint on the mechanism of ultra-high-pressure rock exhumation. Earth and Planetary Science Letters, v. 287, p.116-129.

Buchanan, W. 2008. Tectonic evolution of a Caledonian-aged continental basement eclogite terrane in Liverpool Land, East Greenland. M.Sc. thesis: Auburn, Alabama, University of Auburn.

Faccenda, M., Gerya, T.V., Chakraborty, S. 2008. Styles of post-subduction collisional orogeny: Influence of convergence velocity, crustal rheology and radiogenic heat production. Lithos, v.103, p. 257-287.

Fullsack, P. 1995. An arbitrary Lagrangian–Eulerian formation for creeping flows and its application in tectonic models. Geophysics Journal International, v. 120, p. 1-23.

Gleason, G.C., and Tullis, J. 1995. A flow law for dislocation creep of quartz aggregates determined with the molten salt cell. Tectonophysics, v. 247, p. 1-23.

Hacker, B.R. 1996. Eclogite formation and the rheology, buoyancy, seismicity, and H_2O content of oceanic crust; Subduction top to bottom. Geophysical Monograph, v. 96, p. 337-346.

Hartz, E.H., Andresen, A., Hodges, K.V. and Martin, M.W. 2001. Syncontractional extension and exhumation of deep crustal rocks in the east Greenland Caledonides. Tectonics, v. 20, p. 58-77.

Huismans, R.S., and Beaumont, C. 2003. Symmetric and asymmetric lithospheric extension: relative effects of frictional-plastic and viscous strain softening. Journal of Geophysical Research, v. 108, p. 2496, doi:10.1029/2002JB002026.

Karato, S., Wu, P. 1993. Rheology of the upper mantle; a synthesis. Science, v. 260, p.771-778.

Mackwell, S.J., Zimmerman, M.E., and Kohlstedt, D.L. 1998. High-temperature deformation of dry diabase with application to tectonics on Venus. Journal of Geophysical Research, v. 103, p. 975-984.

Sobolev, S.V., and Babeyko, A.Y. 2005. What drives orogeny in the Andes? Geology, v. 33, p. 617-620.

Walsh, E.O., and Hacker, B.R. 2004. The fate of subducted continental margins; two-stage exhumation of the high-pressure to ultrahigh-pressure Western Gneiss region, Norway. Journal of Metamorphic Geology, v. 22, p. 671–687.

Warren, C.J., Beaumont, C., and Jamieson, R.A. 2008a. Deep subduction and rapid exhumation: Role of crustal strength and strain weakening in continental subduction and ultrahigh-pressure rock exhumation. Tectonics, v. 27, TC6002, doi:10.1029/2008TC002292.

Warren, C.J., Beaumont, C., and Jamieson, R.A. 2008b. Formation and exhumation of ultra-high pressure rocks during continental collision: role of detachment in the subduction channel, Geochemistry Geophysics Geosystems, v. 9, Q04019, doi:10.1029/2007GC001839.

White, A.P., Hodges, K.V., Martin, M.V., and Andresen, A. 2002. Geologic constraints on middle crustal behaviour during synorogenic extension in the East Greenland Caledonides. International Journal of Earth Science, v. 91, p.187-208.

Captions for Figures DR1-DR4, Table DR1, and Animations DR1-DR4

Figure DR1: Summary description of model geometry, boundary conditions, and selected material properties (See DR text, and Table DR1 for detailed description). Black arrows indicate velocity boundary conditions. Red arrows indicate basal heat flux and calculated surface heat flow within the continental interiors. Calculated Moho, base lithosphere, and model base temperatures are shown at right. Key: WQ x *f*, DMD x *f*, WO x *f* are respectively Wet Quartzite, Dry Maryland Diabase and Wet Olivine flow laws scaled by *f*; W is viscous strain weakening factor; φ gives range of frictional-plastic strain softening; A is radioactive heat production (μWm^3) (Beaumont et al., 2009). Material phase change colors show material phase changes and corresponding reference densities at reference temperatures given in Table DR1.

Figure DR2: Detailed Model P results. Blue dashed lines (panel A) indicate PURC boundaries. Red lines (all panels) indicate dominant shear zones and their kinematics. Black lines in panels A and C indicate the original and final positions of the oceanic suture zone respectively. (Ma-pc) refer to time elapsed since collision. PCont is procontinent, RCont is retrocontinent. A) Initial subduction of procontinent margin material to (U)HP conditions, coupled with shallower accretion of procontinent margin sediment. B) Buoyant exhumation of (U)HP margin crust from C to P accomplished by coeval normal-sense shearing at the top of the (U)HP plume and thrust-sense shearing at its base. The emplacement of the plume drives extension at the rear of P coupled with horizontal displacement towards the procontinent. C) Continued but slower exhumation with same kinematics as B driven by subduction of the procontinent interior. The final geometry comprises a large (U)HP dome at the rear of P and a structurally overlying allochthonous nappe stack towards its toe. The suture is highly attenuated and wrapped around the (U)HP dome, separating it from the overlying nappe stack, and much of it has undergone considerable transport towards the procontinent.

Figure DR3: Detailed Model R results. Blue dashed lines (panel A) indicate PURC boundaries. Red lines (all panels) indicate dominant shear zones and their kinematics. Black lines in panels A and C indicate the original and final positions of the oceanic suture zone respectively. Times (Ma-pc) refer to time elapsed since collision. PCont is procontinent, RCont is retrocontinent. A) Initial subduction of procontinent margin material to (U)HP conditions, coupled with shallower accretion of procontinent margin sediment. Minor retrothrusting takes place during this stage. B) Buoyant exhumation of (U)HP margin crust begins in the prowedge mode, transporting material from C to P along coeval normal- and thrust-sense shear zones, the former localized at the P/U boundary. C) The flow of material from P into U initiates major retrothrusting, leading to retrotransport of the exhumed (U)HP crust within R accomplished by coeval normal-sense and thrust-sense shearing, similar to mechanisms proposed for exhumation in the Greenland Caledonides (Hartz et al., 2001; White et al., 2002). The final geometry comprises a prowedge containing an allochthonous nappe stack, an uplifted and extended plug, and a retrowedge containing procontinent (U)HP crust overlying normal retrocontinent crust. The suture is highly attenuated, having been transported both towards P (at the base of the allochthonous nappe stack), and subsequently towards R, where its original tectonostratigraphic position is marked by the contact between the (U)HP procontinent crust and the underlying retrocontinent crust.

Figure DR4: Representative model pressure-temperature (PT) paths for models P, R, and RS. Model RS is similar to Model R but has a slower covergence velocity of 1 cm/a during collision. a) Starting positions of select tracked particles. b) Model P at 25 Ma-pc showing final positions of tracked particles. c) Model R at 25 Ma-pc showing final positions of tracked particles. d) Model RS at 60 Ma-pc, after an approximately equivalent amount of convergence, showing the final positions of tracked particles. e-g) PT plots of tracked particles from models P, R, and RS respectively. Black crosses in f and g represent available constraints on the PT evolution of the Liverpool Land Eclogite Terrane (LLET) from (1) Hartz et al. (2005) and (2) Buchanan (2008). Where no error estimates were provided (e.g., Hartz et al., 2005) errors of 0.5 GPa and 50 ºC were assumed. Representative particles from Model RS achieve peak temperatures similar to those estimated for the LLET. Compared with the models P and R, the higher temperatures achieved by the LLET may be related to slower convergence, resulting in a lower Péclet number owing to longer residence at middle/crustal conditions, or higher values of continental margin heat production (e.g., Warren et al., 2008b). Model RS is hotter and weaker than Model R and may correspond more closely to the Norwegian Caledonides.

Table DR1: Model mechanical and thermal parameters. [a]HP and UHP densities estimated from Hacker (2006) and Walsh and Hacker (2004). [b]Plane strain stress pre-exponential factor (B^*) = $2^{(1-n)/n}\, 3^{-(n+1)/2n}\, A_{uni}^{-1/n}$ where A_{uni} is the laboratory determined uniaxial pre-exponential factor. [c]Retrocontinental margin crust internal angle of friction is 15-2° and 7-2° in models P and R respectively. [d]Retrocontinental margin crust viscosity scaling factor, f, is 3 and 2 in models P and R respectively.

Animation DR1: Animation of Model P showing model materials.

Animation DR2: Animation of Model P showing accumulated strain (see above), plotted as the square root of the second invariant of deviatoric strain.

Animation DR3: Animation of Model R showing model materials.

Animation DR4: Animation of Model R showing accumulated strain (see above), plotted as the square root of the second invariant of deviatoric strain.

Figure DR1

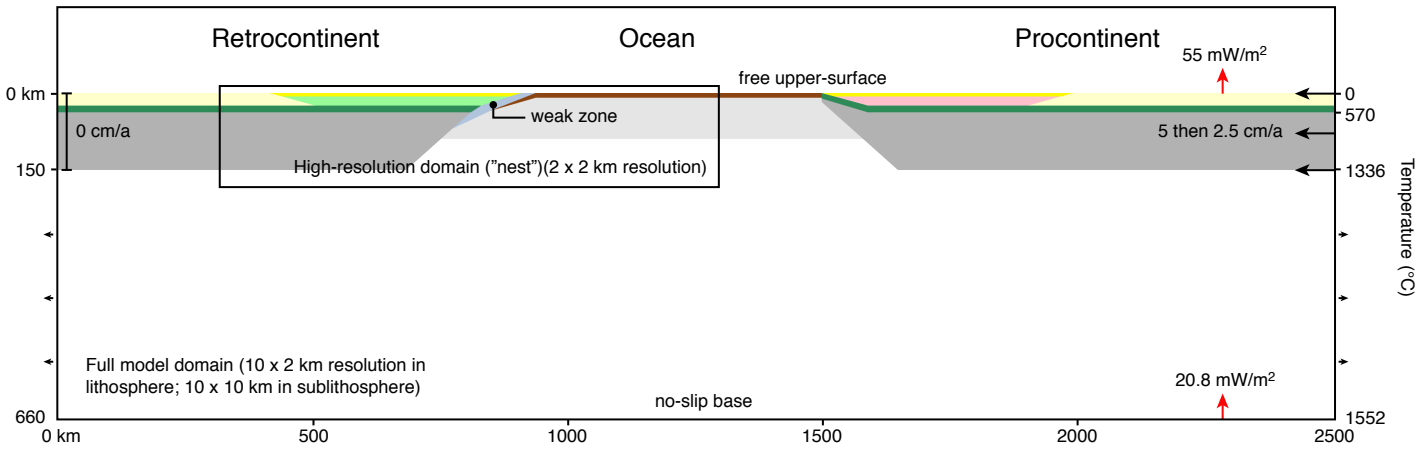

Material colors

- Retro/Pro-margin (WQ*3 (2 in Model R), W 10, φ 15-2° (7-2° in Model R), A 1.5)
- Retro/Pro-interior (WQ*3, W 10, φ 15-2°, A 1.15)
- Lower crust (DMD*0.1, W 10, φ 15-2°, A 0.55)
- Oceanic crust (DMD*0.1, W 10, φ 15-2°, A 0)
- Mantle lithosphere (WO*10, W 0, φ 15-2°, A 0)
- Sublithospheric mantle (WO*0, W 0, φ 15-2°, A 0)

Material phase change colors (in Figs. 2, 3, DR2, DR3, and animations) and reference densities (see Table DR1)

Procontinent margin crust

- Low-pressure (2800 kg/m^3)
- High-pressure (2850 kg/m^3)
- Ultrahigh-pressure (UHP) (2900 kg/m^3)
- Retrogressed UHP (HP) (2850 kg/m^3)
- Retrogressed UHP (2800 kg/m^3)

Procontinent interior crust

- Low-pressure (2800 kg/m^3)
- High-pressure (2850 kg/m^3)

Lower crust

- Low-pressure (2950 kg/m^3)
- High-pressure (3100 kg/m^3)

Oceanic crust

- Low-pressure (2900 kg/m^3)
- High-pressure (3350 kg/m^3)

Figure DR2

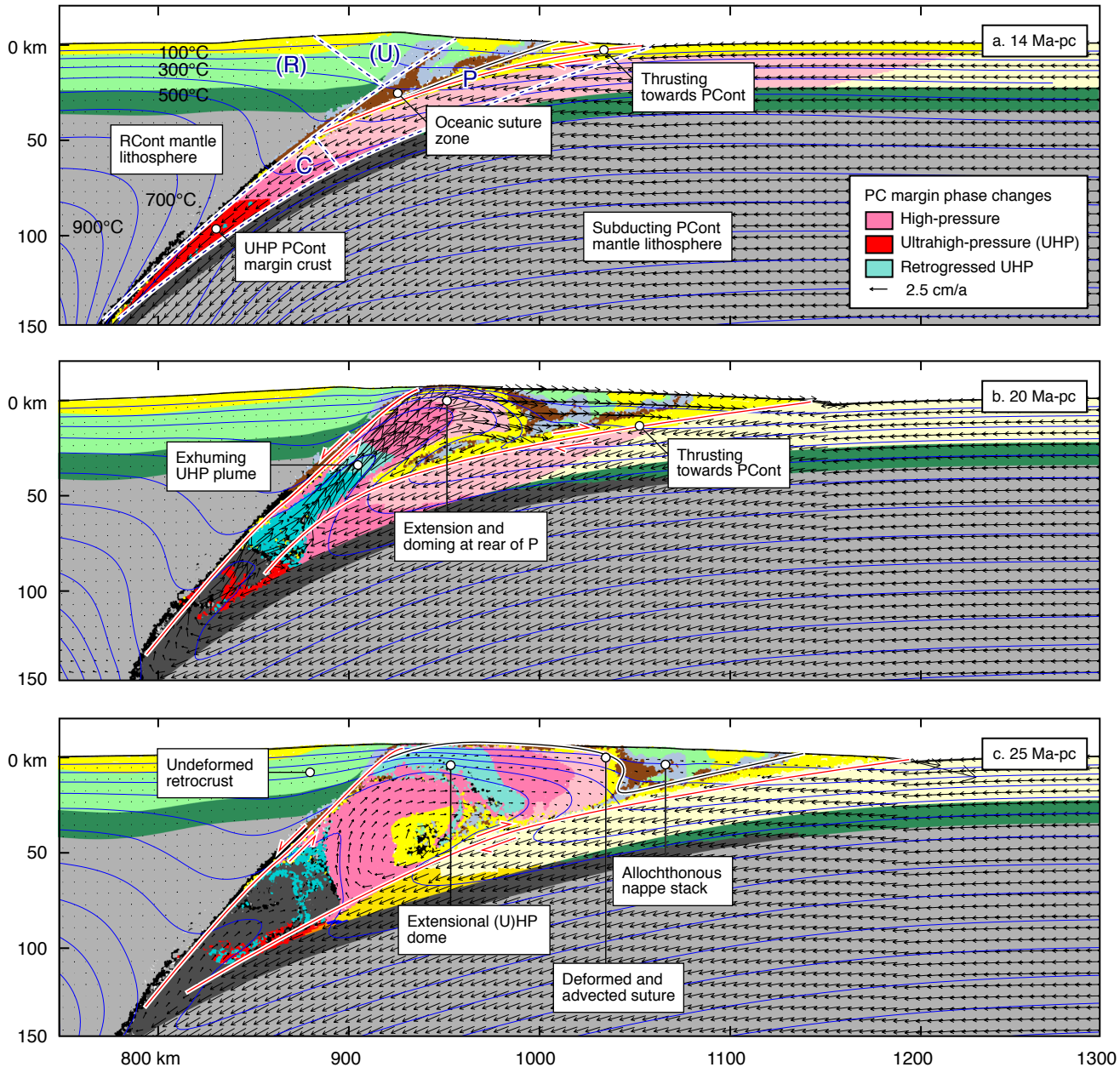
a. 14 Ma-pc
b. 20 Ma-pc
c. 25 Ma-pc
0 km
50
100
150
100°C
300°C
500°C
700°C
900°C
(R)
(U)
P
C
RCont mantle lithosphere
Oceanic suture zone
Thrusting towards PCont
Subducting PCont mantle lithosphere
UHP PCont margin crust
PC margin phase changes
High-pressure
Ultrahigh-pressure (UHP)
Retrogressed UHP
2.5 cm/a
Exhuming UHP plume
Thrusting towards PCont
Extension and doming at rear of P
Undeformed retrocrust
Allochthonous nappe stack
Extensional (U)HP dome
Deformed and advected suture
800 km
900
1000
1100
1200
1300

Figure DR3

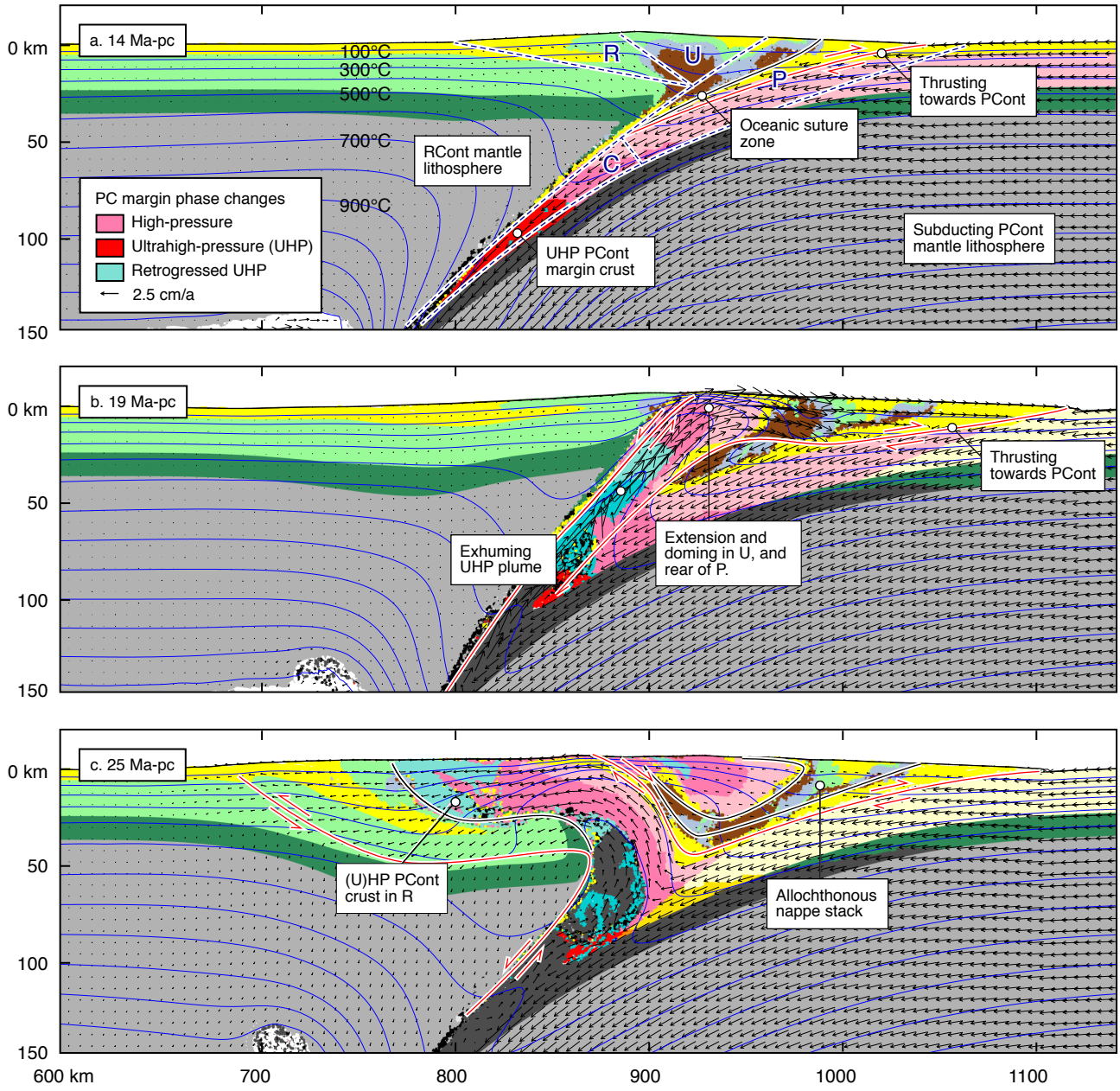
a. 14 Ma-pc
100°C
300°C
500°C
700°C
900°C
R
U
P
C
Thrusting towards PCont
Oceanic suture zone
RCont mantle lithosphere
Subducting PCont mantle lithosphere
UHP PCont margin crust
PC margin phase changes
High-pressure
Ultrahigh-pressure (UHP)
Retrogressed UHP
2.5 cm/a
b. 19 Ma-pc
Thrusting towards PCont
Exhuming UHP plume
Extension and doming in U, and rear of P.
c. 25 Ma-pc
(U)HP PCont crust in R
Allochthonous nappe stack
0 km
50
100
150
600 km
700
800
900
1000
1100

Figure DR4

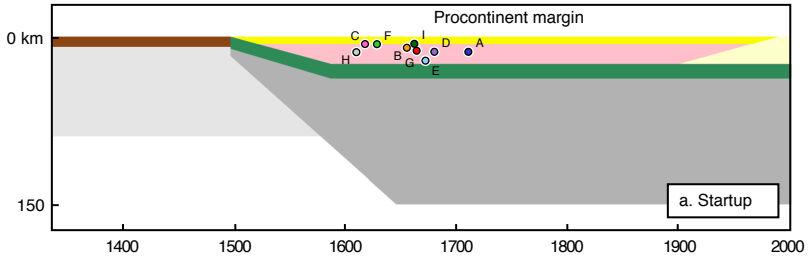

Model P (Prowedge mode)

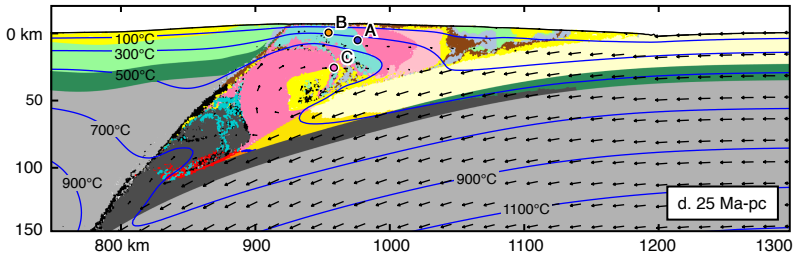

Model R (Retrowedge mode)

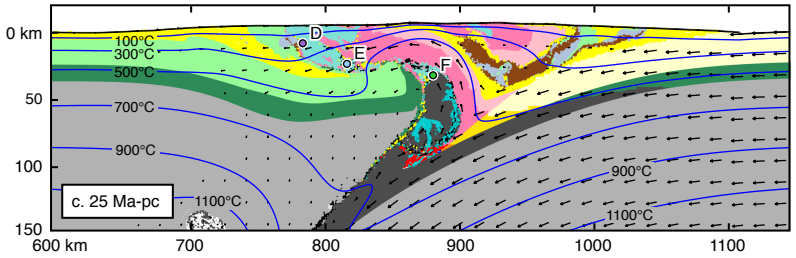

Model RS (Retrowedge mode with convergence rate of 1 cm/a)

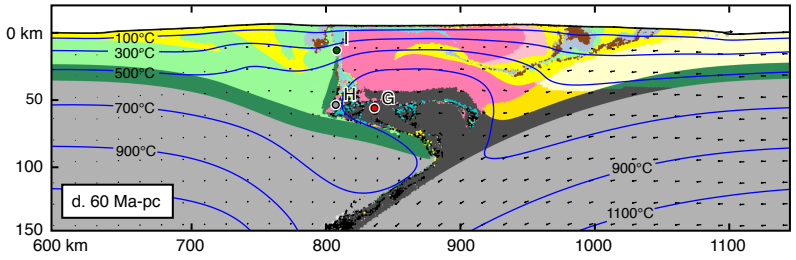

e. Model P PT paths (end at 25 Ma-pc)

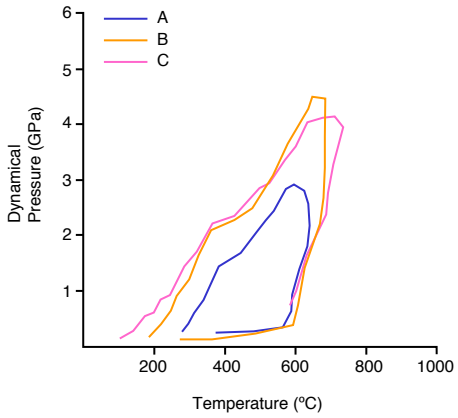

f. Model R PT paths (end at 25 Ma-pc)

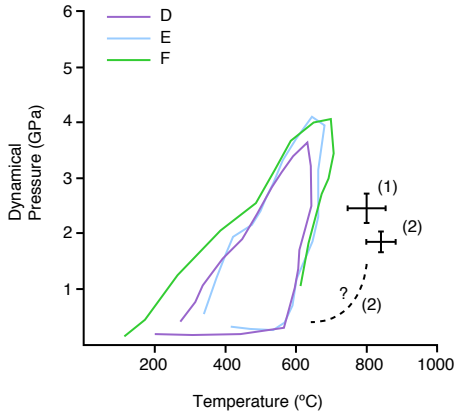

g. Model RS PT paths (end at 60 Ma-pc)

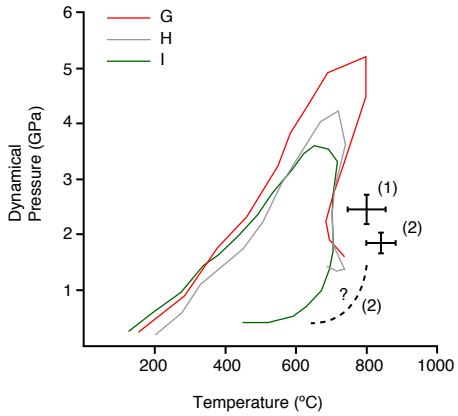

TABLE DR1: MODEL THERMAL/MECHANICAL PARAMETERS

	Units	RC interior crust	RC margin crust	PC margin crust	PC interior crust	Lower crust	Oceanic crust	Continental mantle lithosphere	Oceanic mantle lithosphere	Sublithospheric mantle
Mechanical Parameters										
Thickness (max.)	km	24	24	24	24	12	8	114	82	to 660 km depth
Reference density	kg m^{-3}	2800	2800	2800	2800	2950	2900	3250	3250	3250
Reference density T	K	473	473	473	473	773	273	1609	1609	1609
Reference density HP[†]	kg m^{-3}	2850	2850	2850	2850	3100	3350	-	-	-
Reference density UHP[†]	kg m^{-3}	2900	2900	2900	2900	3100	3350	-	-	-
Effective internal angle of friction (φ_{eff})	deg	15-2	15-2, 8-2[#]	15-2	15-2	15-2	15-2	15-2	15-2	15-2
Cohesion	MPa	2	2	2	2	0	0	0	0	0
Flow law	-	WQ	WQ	WQ	WQ	DMD	DMD	WO	WO	WO
Viscosity scaling factor *(f)*	-	5	3, 2[††]	3	5	0.1	0.1	10	10	1
Strain weakening factor *(Ws)*	-	10	10	10	10	10	10	1	1	1
n		4	4	4	4	4.7	4.7	3	3	3
B^*[§]	Pa $s^{1/n}$	2.92×10^6	2.92×10^6	2.92×10^6	2.92×10^6	1.91×10^5	1.91×10^5	1.92×10^4	1.92×10^4	1.92×10^4
Q	kJ mol^{-1}	223	223	223	223	485	485	430	430	430
V^*	m^3 mol^{-1}	0	0	0	0	0	0	1×10^{-5}	1×10^{-5}	1×10^{-5}
Thermal Parameters										
Heat capacity	m^2 s^{-2} K^{-1}	750	750	750	750	750	750	1250	1250	1250
Thermal Conductivity	W m^{-1} K^{-1}	2.25	2.25	2.25	2.25	2.25	2.25	3	2.25	52
Thermal diffusivity	m^2 s^{-1}	1×10^{-6}	1×10^{-6}	1×10^{-6}	1×10^{-6}	1×10^{-6}	1×10^{-6}	0.7×10^{-6}	0.6×10^{-6}	1.4×10^{-5}
Thermal expansion	K^{-1}	3×10^{-5}	3×10^{-5}	3×10^{-5}	3×10^{-5}	3×10^{-5}	3×10^{-5}	3×10^{-5}	3×10^{-5}	3×10^{-5}

Heat production	$\mu W\ m^{-3}$	1.15	1.5	1.5	1.15	0.55	0	0	0	0

RCont is retrocontinent; PCont is procontinent. WQ is wet quartzite; DMD is dry Maryland diabase; WO is wet olivine.

[†]HP and UHP densities based on Hacker (1996) and Walsh and Hacker (2004).

[§] B^* (plane strain stress pre-exponential factor) = $2^{(1-n)/n}\ 3^{-(n+1)/2n}\ A_{uni}^{\ -1/n}$, where A_{uni} is the uniaxial pre-exponential factor.

[#]Internal angle of friction for RCont margin crust in Model P is 15-2, and 7-2 in Model R.

[††]Viscous scaling factor (f) for RCont margin crust in Model P is 3, and 2 in Model R.